

## Article

# Design of V<sub>2</sub>O<sub>5</sub> Blocks Decorated with Garlic Peel Biochar Nanoparticles: A Sustainable Catalyst for the Degradation of Methyl Orange and Its Antioxidant Activity

Perumal Sarojini<sup>1</sup>, Karuppasamy Leeladevi<sup>1</sup>, Thavuduraj Kavitha<sup>1</sup>, Krishnamoorthy Gurushankar<sup>2</sup>, Ganesan Sriram<sup>3,\*</sup>, Tae Hwan Oh<sup>3,\*</sup> and Karthik Kannan<sup>4,5,\*</sup>

- <sup>1</sup> Department of Chemistry, Sri S. Ramasamy Naidu Memorial College, Sattur 626203, Tamil Nadu, India; sarojinismcchemistry@gmail.com (P.S.); leela232323@gmail.com (K.L.); tkavitha@srrmcollege.ac.in (T.K.)
- <sup>2</sup> Department of General Pathology, Saveetha Dental College and Hospitals, Saveetha University, Saveetha Institute of Medical and Technical Sciences (SIMATS), Chennai 600077, Tamil Nadu, India; gurushankar01051987@gmail.com
- <sup>3</sup> School of Chemical Engineering, Yeungnam University, Gyeongsan 38541, Republic of Korea
- <sup>4</sup> Chemical Sciences Department and The Radical Research Centre, Ariel University, Ariel 40700, Israel
- <sup>5</sup> Australian Center for Sustainable Development Research and Innovation (ACSDRI), Unit 36/21 South Tce, 9 Adelaide, SA 5000, Australia
- \* Correspondence: sriramyu@yu.ac.kr (G.S.); taehwanoh@ynu.ac.kr (T.H.O.); karthikkannanphotochem@gmail.com (K.K.)

**Abstract:** In this study, novel V<sub>2</sub>O<sub>5</sub>-decorated garlic peel biochar (VO/GPB) nanocomposites are prepared via the facile hydrothermal technique. As-synthesized VO/GPB is characterized by various spectroscopic and analytical techniques. The surface morphology of the as-prepared samples was predicted by SEM analysis, which shows that the block-like V<sub>2</sub>O<sub>5</sub> was uniformly decorated on the stone-like GPB surface. The elemental mapping analysis confirms the VO/GPB composite is composed of the following elements: C, O, Na, Mg, Si, P, K, and V, without any other impurities. The photocatalytic activity of the VO/GPB nanocomposite was examined by the degradation of methyl orange (MO) under the irradiation of visible light; 84% degradation efficiency was achieved within 30 min. The reactive oxidative species (ROS) study reveals that hydroxyl and superoxide radicals play an essential role in MO degradation. Moreover, the antioxidant action of the VO/GPB nanocomposite was also investigated. From the results, the VO/GPB composite has higher antioxidant activity compared to ascorbic acid; the scavenging effect increased with increasing concentrations of VO/GPB composite until it reached 40 mg/L, where the scavenging effect was the highest at 93.86%. This study will afford innovative insights into other photocatalytic nanomaterials with effective applications in the field of photocatalytic studies with environmental compensation.

**Keywords:** VO/GPB; methyl orange; visible light; stability; photodegradation; antioxidant



**Citation:** Sarojini, P.; Leeladevi, K.; Kavitha, T.; Gurushankar, K.; Sriram, G.; Oh, T.H.; Kannan, K. Design of V<sub>2</sub>O<sub>5</sub> Blocks Decorated with Garlic Peel Biochar Nanoparticles: A Sustainable Catalyst for the Degradation of Methyl Orange and Its Antioxidant Activity. *Materials* **2023**, *16*, 5800. <https://doi.org/10.3390/ma16175800>

Academic Editor: Aivaras Kareiva

Received: 29 July 2023

Revised: 19 August 2023

Accepted: 21 August 2023

Published: 24 August 2023



**Copyright:** © 2023 by the authors. Licensee MDPI, Basel, Switzerland. This article is an open access article distributed under the terms and conditions of the Creative Commons Attribution (CC BY) license (<https://creativecommons.org/licenses/by/4.0/>).

## 1. Introduction

A growing concern at the current time is the release of organic contaminants into the water system. The large scale of untreated wastewater from pharmaceutical industries and agricultural activities, including mineral gases and volatile and semi-volatile organic hydrocarbons, are sources of environmental pollution [1–3]. Worldwide, people are regularly exposed to a wide range of toxic pollutants. These kinds of toxic pollutants cause contamination in air, food, and drinking water. Organic pollutants from human and animal waste, as well as industrial byproducts, can affect aquatic creatures and microbes if they are not properly treated before being released into the environment. Azo-containing complexes account for over 70% of the dye family [4–6]. Among them, methyl orange (MO) is broadly utilized in foodstuffs, paper, leather industries, and textiles. Because of the improper release of MO in the ecosystem, the contamination of water bodies is highly

increased; it must be removed from water bodies, owing to its toxicity [7–9]. These kinds of challenging problems increase the need for green, as well as highly effective, methodologies to eliminate toxic pollutants from the environment. Typical analytical methods like ozonation, membrane separation, sonolysis, and coagulation are often inadequate in the handling of vast, new, emerging micro-pollutants [10,11].

Photocatalysis is a subject that combines the topics of energy research, nanotechnology, environmental science, photonics, material science, chemical analysis, and so on [12]. Recently, semiconductors have generally been chosen as photocatalysts, since they have a narrow bandgap between the valence and conduction bands. Changing and promoting emergent technology leads to decreased contamination in air and water [13–15]. This is the best green approach for furnishing everyone in the world. Semiconductor catalysts are favored in the photocatalytic degradation of wastewater for the following reasons: (i) they are economical; (ii) their non-toxicity; (iii) they show accommodating properties that can be modified by doping, size tailoring, or sensitizers; (iv) they afford the ability for a multi-electron relocate process; and (v) they are able to enlarge their utilization without considerable loss in the photocatalytic application [16–18].  $\text{TiO}_2$  and  $\text{ZnO}$  are well known to be excellent photocatalysts for the degradation of numerous environmental contaminants, owing to their elevated photosensitivity. The most important drawback of  $\text{TiO}_2$  and  $\text{ZnO}$  is the larger bandgap at 3.2 eV ( $\sim 388$  nm) [19,20]. Because of their large bandgap values,  $\text{TiO}_2$  and  $\text{ZnO}$  act only in the presence of UV light, with wavelengths shorter than 380 nm.

Recently, various metal oxide nanomaterials have been used for environmental applications [21–23]. Among them,  $\text{V}_2\text{O}_5$ -based nanomaterials have been synthesized and utilized in a miscellany of applications. Moreover,  $\text{V}_2\text{O}_5$  is an effective n-type semiconductor photocatalyst for the catalytic degradation of hazardous pollutants, due to its harmless nature, morphology, and simulated sunlight absorption [24–26]. Due to its quick electron–hole recombination and limited stability, bare  $\text{V}_2\text{O}_5$  is inadequate to meet the realistic necessities in photocatalytic applications [27]. The inclusion or doping of various metals, semiconductors, or other suitable elements to improve the catalytic stability of  $\text{V}_2\text{O}_5$  is an excellent alternative [28,29].

Production of carbon-based nanomaterials, i.e., biochar nanocomposites, has resulted from the combination of biochar technology and nanobiotechnology. Improved physical, chemical, and surface qualities can be found in nanosized biochar material. Among its many uses, it can be a soil amendment, an effluent purification aid, a bioremediation substrate, a plant disease surveillance tool, and a support substance for inhibiting enzymes. Its low price, long lifespan, and low impact on the surroundings make it a strong contender to replace more established methods. The retention of biochar is another way it helps with climate change mitigation. Because of its mobility in soil and superior absorption capacity, biochar could be a viable alternative for disposing of waste. Biochar is a thermally processed biomaterial that is made from plant waste through pyrolysis and serves as a vital supporting material. It is a charcoal-like material with a specific morphology and a large surface area that provides better catalytic activity against organic pollutants [30–32]. For these and other reasons, biochar is increasingly being included in nanocomposites [17,33–37] for applications like wastewater treatment, energy generation, and the adsorption of organic dyes and other pollutants. Its porous structure, increased number of exterior functional groups, and better surface area-to-volume ratio make it a successful material for enzymes [38]. Biochar is a cost-effective and environmentally sustainable material that exhibits exceptional efficiency and can be easily produced. Wastewater treatment has garnered heightened attention. Biochar possesses several characteristics that render it a good material for pollution treatment. These include its high surface area, high porosity, presence of sufficient functional surface groups, exceptional ion exchange ability, and remarkable stability. Furthermore, the synergistic interaction between biochar and various metals or metal oxides has the potential to augment the adsorption capability, amplify the absorption of visible light, facilitate the separation of photogenerated electrons

and holes, diminish the band gap, and, ultimately, enhance the photocatalytic efficacy of catalysts based on biochar. Extensive research has been conducted on the utilization of biochar and biochar-based products for the remediation of environmental contaminants [39–41].

In this work, VO/GPB nanocomposite was prepared by a typical hydrothermal method. The VO/GPB catalyst was analyzed by X-ray Powder Diffraction (XRD), Ultraviolet–Visible Diffuse Reflectance Spectroscopy (UV-DRS), Scanning Electron Microscopy (SEM) with Energy-dispersive X-ray spectroscopy (EDAX), and photoluminescence. Due to their remarkable physical and chemical characteristics, VO/GPB metal oxide nanostructures find widespread application. These include, but are not limited to, biomedical applications, the conversion of carbon dioxide, the photocatalytic destruction of organic pollutants, the purification of pollutants such as heavy metals, the identification of hazardous gases, the surface treatment of fabrics for use in wearable electronic gadgets, and the filtration of heavy metals from the environment. Due to their inexpensiveness, durability, effectiveness, and limited influence on the atmosphere, these types of metal oxides are widely recognized as materials for the remediation of environmental damage. Metal oxides are promising for environmental remediation because of their high catalytic capability when driven by visible light. Metal oxides' electrical structure, light-absorbing properties, charge-transport mechanisms, and enhanced lifetimes all work together to make them good photocatalysts. This research looks at the recent trends and possible future possibilities for using metal oxides as photocatalysts in the fields of energy and the environment. In addition, it provides a thorough evaluation of the state of the industry, the challenges it faces, and the potential for expansion. Taking these factors into account, we developed VO/GPB nanocomposites that are inexpensive, extremely effective, lightweight, and kind to the environment. In just 30 min, the photocatalytic degradation efficiency of MO dye was increased to almost 84% under visible light irradiation. In photocatalytic applications, the VO/GPB nanocomposite has shown remarkable degrading efficacy and high stability. This is the first publication to our knowledge to discuss the use of VO/GPB nanocomposites as a photocatalyst for the degradation of MO dye, and the results show significantly higher degradation efficiency values than those shown in previous studies. Additionally, the antioxidant activity of the VO/GPB nanocomposite was studied to predict its ability to scavenge the hydroxyl radical. Therefore, it gives researchers in this field new information to consider.

## 2. Materials and Methods

Analytical grade ammonium metavanadate ( $\text{NH}_4\text{VO}_3$ )  $\geq 99.0\%$ , cetyl trimethyl ammonium bromide (CTAB)  $\geq 98\%$ , sodium hydroxide (NaOH)  $\geq 98\%$ , methyl orange (MO) 85%, benzoquinone (BQ)  $\geq 98\%$ , triethanolamine (TEA)  $\geq 99\%$ , and isopropyl alcohol (IPA)  $\geq 99.7\%$  were purchased from Sigma-Aldrich (St. Louis, MO, USA). All other chemicals and reagents were analytical grade and used without further purification. All the required solutions were prepared with distilled water.

### 2.1. Preparation of Garlic Peel Biochar (GPB)

The garlic was collected in a single batch from a local store in Krishnankoil, Tamil Nadu, India. After collection, the garlic was peeled, cleaned, and dried overnight at  $110\text{ }^\circ\text{C}$ . The dried peels were pulverized to obtain a fine powder. The powdered garlic peel was subjected to calcination at  $580\text{ }^\circ\text{C}$  for 6 h. As prepared, garlic peel biochar was named GPB.

### 2.2. Preparation of $\text{V}_2\text{O}_5$ /Garlic Peel Biochar (VO/GPB) Composite

In a simple hydrothermal method, 0.1 mol of  $\text{NH}_4\text{VO}_3$  and 0.1 mol of  $\text{C}_{19}\text{H}_{42}\text{BrN}$  were completely dissolved in 100 mL of distilled water with continuous stirring for 1 h. NaOH was used to adjust the pH of the solution to 10. Consequently, 0.5 g of GPB was mixed with the above solution. This solution was allowed to undergo ultra-sonification for 30 min. Then, after stirring, the mixture was placed in a Teflon-lined autoclave and heated to  $140\text{ }^\circ\text{C}$  for 12 h. Water and ethanol were used to wash and centrifuge the final

product. Finally, the VO/GPB composite was calcined at 650 °C for 3 h. Figure 1 shows the schematic representation of the preparation of the VO/GPB composite.

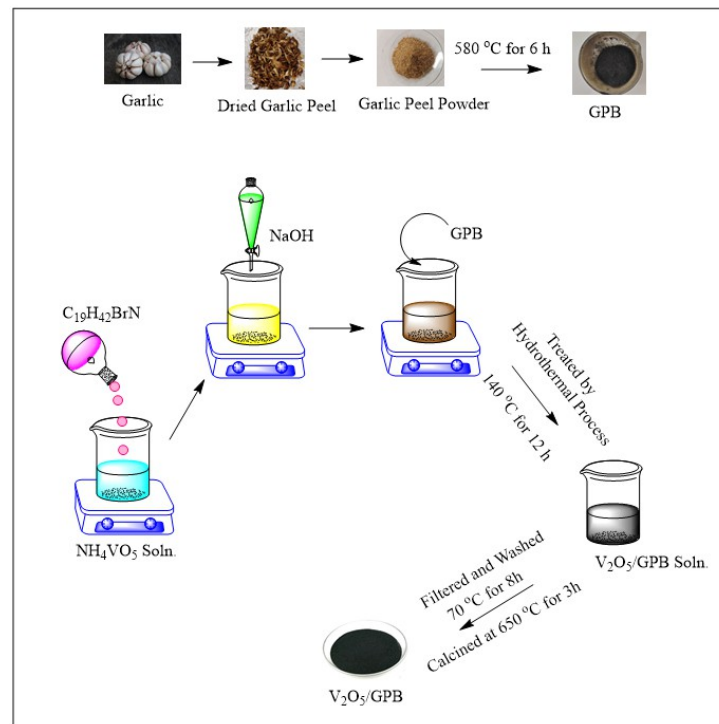


**Figure 1.** Schematic representation of preparation of VO/GPB composite.

### 2.3. Characterization Technique

The XRD patterns of VO/GPB samples were analyzed using a Bruker-D8 Advance ECO X-ray diffractometer (Shimadzu Corporation, Kyoto, Japan). The IR Tracer-100 FT-IR spectrophotometer was used to examine the Fourier-transform infrared spectroscopy (FT-IR) spectrum (Jasco, Tokyo, Japan). The morphology of the VO/GPB samples was recorded by EVO18-CARL ZEISS (Oberkochen, Germany) Scanning Electron Microscopy. The UV–Visible–Diffuse Reflectance Spectrum (UV-DRS) was predicted by Shimadzu UV-2600 (Shimadzu Corporation, Kyoto, Japan), in which BaSO<sub>4</sub> was used as reference material. The photoluminescence was analyzed by RF-6000 (Shimadzu Corporation, Kyoto, Japan). The UV-1800 Shimadzu UV–visible spectra were utilized to analyze the concentration of the photodegradation solution. Origin 8.5 software was used to draw a plot in this work.

### 2.4. Photocatalytic Experiments

The photocatalytic action of VO/GPB was estimated by MO degradation under the illumination of visible light equipped with a tungsten incandescent lamp (500 W). Consequently, 40 mg/L of the VO/GPB nanocomposite was dissolved in 100 mL of distilled water with a 30 mg/L concentration of MO. Then, the solution was stirred for 30 min to maintain adsorption–desorption equilibrium. The above solution was placed in a reaction chamber. At a specific interval, an aliquot sample was collected, and the catalyst was excreted through an ultracentrifuge. The supernatant solutions were analyzed by a UV–Visible spectrophotometer to identify the concentration of the solution. At last, the VO/GPB nanocomposite was collected for the repeatability test. In addition, the photocatalytic degradation efficiency of VO/GPB was calculated by the following equation:

$$\text{Photodegradation efficiency (\%)} = (C_0 - C/C_0) \times 100$$

where  $C_0$  and  $C$  correspond to the initial and final concentration of MO dye before and after irradiation.

### 2.5. Antioxidant Activity by DPPH Assay

The antioxidant behavior of the VO/GPB nanocomposite was examined by the 1-1-diphenyl-2-picryl-hydrazyl (DPPH) free radical scavenging activity. For this, 0.2  $\mu\text{M}$  of 2,2-diphenyl-1-picrylhydrazyl (DPPH) solution was prepared with methanol. Then, 3 mL of VO/GPB nanocomposite (20–40 mg/L) was added to the methanolic solution of DPPH with continuous stirring for 30 min under dark conditions. The absorbance of the above mixture was calculated at 517 nm using a UV-1800 Shimadzu UV/Vis spectrophotometer. The percentage of free radical scavenging activity was measured by the following calculation:

$$\text{Scavenging activity (\%)} = \{(A_0 - A_1)/A_0\} \times 100 \quad (1)$$

where  $A_0$  and  $A_1$  are the absorbances of the control and sample, respectively.

## 3. Results and Discussion

### 3.1. XRD Analysis

The crystalline structure and phase purity of synthesized  $\text{V}_2\text{O}_5$ , GPB, and VO/GPB composite were examined using Powder X-ray Diffraction (PXRD) analysis, as depicted in Figure 2. The Powder-XRD (PXRD) patterns of pristine  $\text{V}_2\text{O}_5$  were perfectly matched with standard JCPDS Card No. 41-1426 [42]. It showed peaks at  $2\theta$  values of 15.37, 20.26, 21.95, 26.34, 30.72, 32.41, 34.45, 41.18, 45.56, 47.43, 51.13, 55.85, 58.90, 60.77, 62.10, 65.97, 72.05, and 74.43°, corresponding to (200), (001), (101), (110), (400), (011), (310), (002), (411), (600), (302), (601), (021), (321), (710), (103), (303), and (503), confirming the crystalline nature of  $\text{V}_2\text{O}_5$ . The VO/GPB composite had major PXRD peaks for  $\text{V}_2\text{O}_5$  and GPB. Moreover, the orientation of the peak was shifted to a higher intensity due to doping with GPB. This proves the successful formation of VO/GPB nanocomposite. There was no other peak from impurities, showing the purity of the prepared samples.

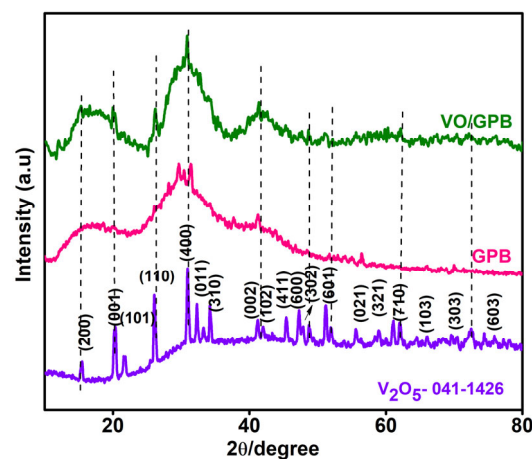


**Figure 2.** XRD patterns of  $\text{V}_2\text{O}_5$ , GPB, and VO/GPB nanoparticles.

### 3.2. Morphological Analysis

The morphological analysis of  $\text{V}_2\text{O}_5$ , GPB, and VO/GPB composite was performed using Scanning Electron Microscopy (SEM) analysis. As shown in Figure 3a, the SEM revealed that the bare  $\text{V}_2\text{O}_5$  nanomaterials exhibited a block-like structure as surface morphology. This demonstrates that they were nanometer-sized, and Figure 3b reveals the stone-like GPB morphology structure, which was well agglomerated.

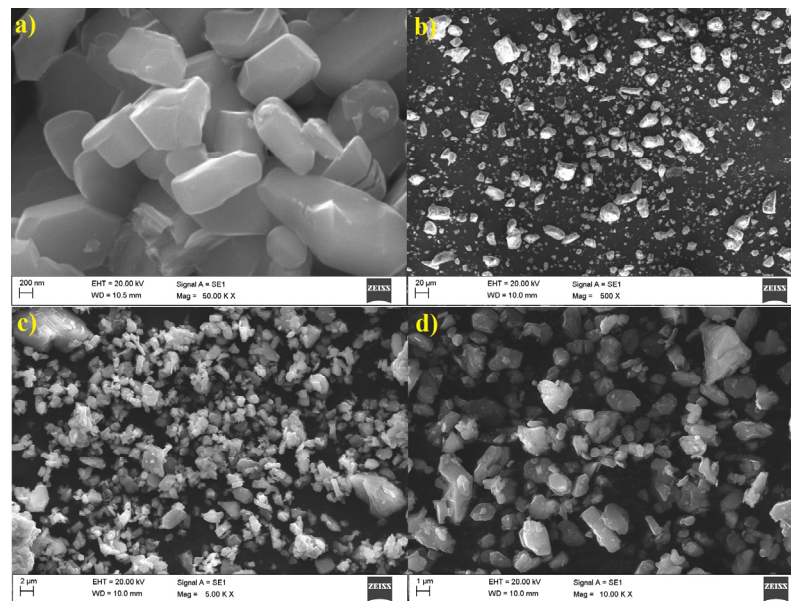


**Figure 3.** SEM image of as-prepared (a)  $V_2O_5$  nanoparticles captured at  $\times 50,000$  (scale bar 200 nm), (b) GPB captured at  $\times 500$  (scale bar 20  $\mu m$ ) and (c,d) VO/GPB nanocomposite captured at  $\times 5000$  (scale bar 2  $\mu m$ ) and  $\times 10,000$  (scale bar 1  $\mu m$ ) at different magnifications.

Figure 3c,d demonstrates the different magnifications of the VO/GPB composite: the  $V_2O_5$  was finely dispersed in GPB stones in the composite structure. The size of the VO/GPB composite ranged from 200 nm to 1  $\mu m$ . Furthermore, EDAX (Figure 4) analysis was used to estimate the total weight of the different elemental compositions presents in the VO/GPB nanocomposite. The results of EDAX and elemental mapping analysis (Figure 5a–h) confirmed that the VO/GPB composite was composed of C, O, Na, Mg, Si, P, K, and V, without any other impurities. Additionally, the weight percentages of the elements present in the composite were 6.8, 23.4, 0.9, 1.4, 1.4, 3.4, 3.2, and 59.5 wt.%, respectively.

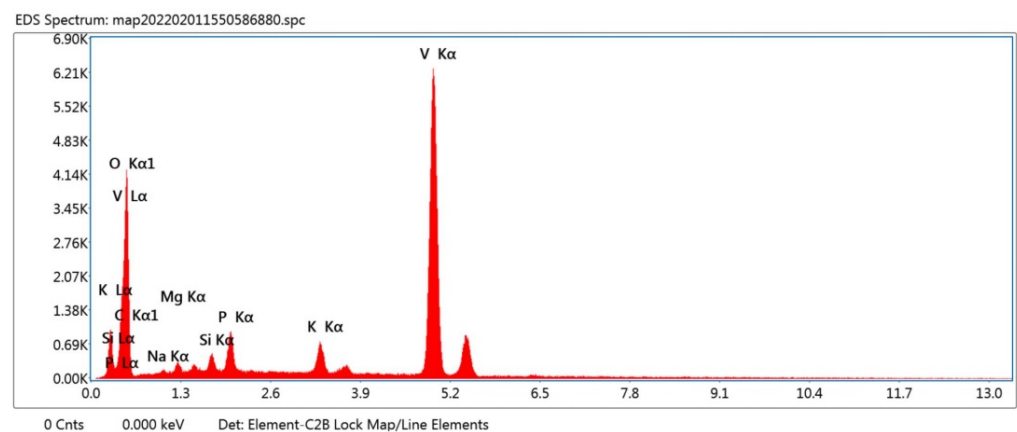


**Figure 4.** EDAX spectrum of as-prepared VO/GPB composite.

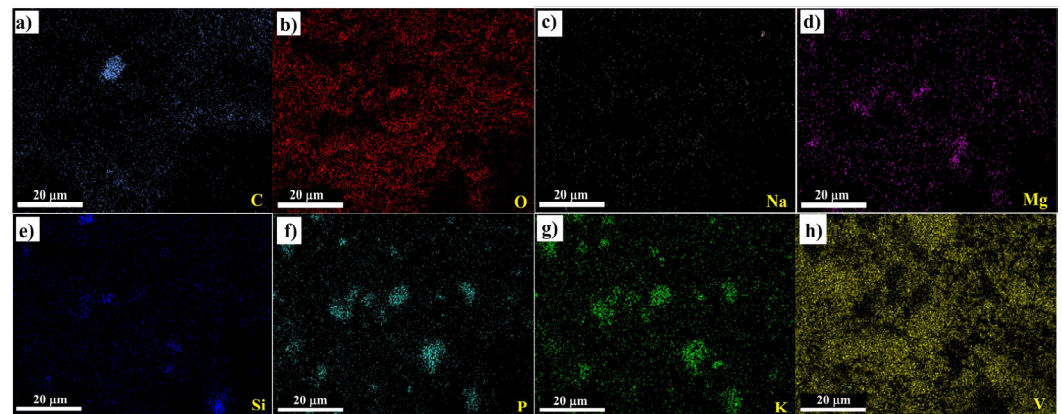


**Figure 5.** Elemental mapping images with a magnification of  $\times 500$  (scale bar  $20\ \mu\text{m}$ ) of VO/GPB composite. The color mapping analysis of various components (a) C, (b) O, (c) Na, (d) Mg, (e) Si, (f) P, (g) K and (h) V.

### 3.3. Optical Properties

The UV-DRS analysis was used to estimate the bandgap value for the  $\text{V}_2\text{O}_5$  nanoblocks, GPB grits, and VO/GPB composite, and also to predict the irradiation source for the photocatalytic degradation. A bandgap value plays an important role in this photocatalytic process [43]. Based on this, the catalysts absorb light energy and initiate the recombination of electron ( $e^-$ )–hole ( $h^+$ ) pairs [44,45]. From Figure 6a, the VO/GPB composite had an absorption value of nearly 500 nm; this high absorption wavelength proved that the photocatalytic degradation should perform well under visible light source irradiation. As shown in Figure 6b, Tauc's plots equation was utilized to identify the band energy values of the  $\text{V}_2\text{O}_5$  nanoblocks and VO/GPB composite, which were 1.71 and 1.49 eV, respectively. The bandgap values of VO/GPB were reduced by combining them with GPB biochar in the  $\text{V}_2\text{O}_5$  sample. The visible light photocatalytic activity of the nanocomposite is enhanced by the incorporation of biochar due to the reduction in the overall optical bandgap and the minimization of the electron–hole ( $e-h$ ) recombination rate. And finally, it prevents photo-induced electron–hole pairs from recombining and speeds up the electron transfer process from photocatalyst particles to reactive sites. While  $\text{V}_2\text{O}_5$  has a band gap energy of about 1.71 eV, for VO/GPB, the value was only reduced to the 1.49 eV range when biochar was also included.

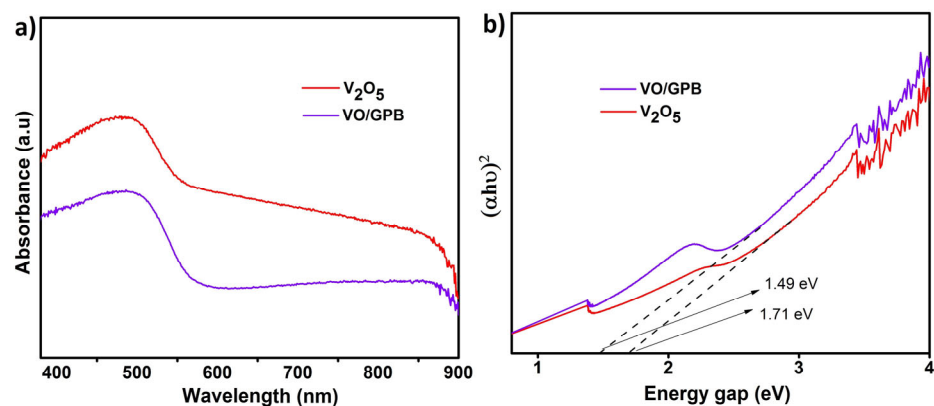


**Figure 6.** Optical properties of samples: (a) UV-Vis diffused reflectance spectra of as-prepared  $\text{V}_2\text{O}_5$  and VO/GPB samples, and (b) the bandgap energy values of  $\text{V}_2\text{O}_5$  and VO/GPB nanocomposite.

### 3.4. Photoluminescence Studies

The Photoluminescence (PL) spectrum of  $\text{V}_2\text{O}_5$  nanoblocks and VO/GPB composite is displayed in Figure 7. PL analysis is used to estimate the charge separation between photo-generated  $e^- - h^+$  pairs. The  $\text{V}_2\text{O}_5$  nanoblocks show an excitation peak at 520 nm,

owing to the recombination of the  $e^- - h^+$  pair. But the VO/GPB composite exhibited a lower intensity peak than the  $V_2O_5$  nanoblocks due to the lower recombination of charge carriers. This lesser charge separation of  $e^- - h^+$  pairs improves the lifetime of the charge carriers and increases the catalytic efficiency of the VO/GPB composite.

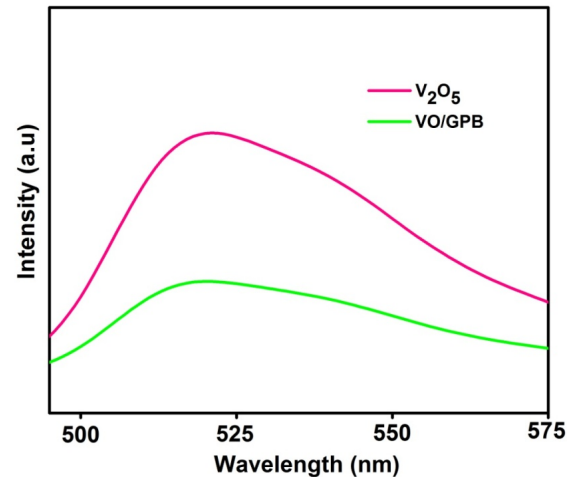


**Figure 7.** The Photoluminescence spectra of the as-prepared  $V_2O_5$  and VO/GPB samples.

### 3.5. Estimation of the Photodegradation Process

#### 3.5.1. The Effectiveness of the Diverse Catalyst

The catalytic activity of the  $V_2O_5$  nanoblocks, GPB grits, and VO/GPB composite were examined by the degradation of methyl orange (MO—30 mg/L) by irradiation with visible light. The photodegradation absorption spectra of MO are shown in Figure 8a. In the degradation process, the electron–hole pairs are generated by the illumination of light; after 30 min of irradiation, the concentration of MO slowly diminished to almost zero. The VO/GPB composite showed degradation efficiency of up to 84%. Based on this process, the effects of  $V_2O_5$  nanoblocks, GPB grits, and VO/GPB composite catalytic materials were predicted. As shown in Figure 8b, the VO/GPB composite possesses a superior catalytic efficiency than the bare  $V_2O_5$  nanoblocks and GPB grits, owing to the lower energy gap value and considerable light absorption in the visible region. Moreover, the optimal parameters like catalyst loading and dye concentration for the photodegradation process were considered to organize the optimal conditions for the degradation of MO.

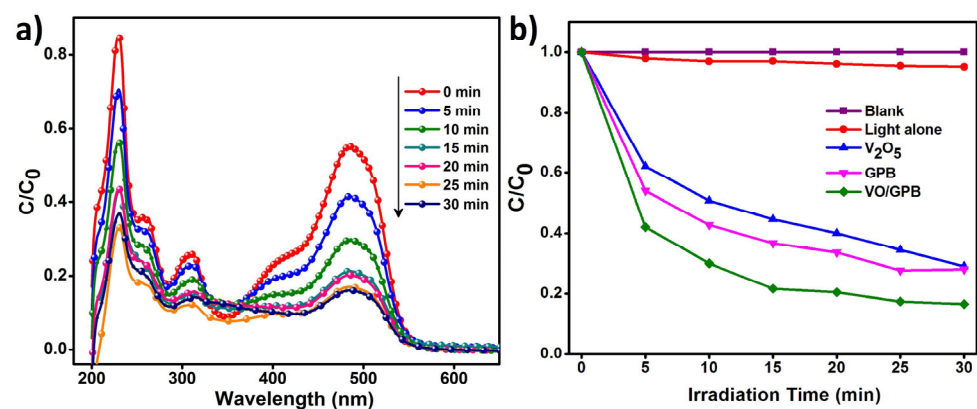


**Figure 8.** Photodegradation of MO solution under different conditions: (a) Absorption spectrum for photodegradation of aqueous MO solution under visible light irradiation in the presence of 40 mg VO/GPB catalyst and (b) Photocatalytic degradation of MO dye of different samples under visible light irradiation.



### 3.5.2. The Effectiveness of Catalyst Dosage

The MO degradation (40 mg/L) with  $V_2O_5$  nanoblocks, GPB grits, and VO/GPB composite was carried out to find the absorption wavelength under identical conditions. Figure 9a demonstrates the photodegradation of MO when altering the catalyst dose from 20 to 50 mg. Among these values, 40 mg of catalyst was adequate for superior degradation. Additionally, increasing the catalyst dose from 40 to 50 mg decreased the degradation efficacy due to the permeation of light sources into the reaction solution being restricted by the lowest amount of photosynthetic charge carrier production. Thus, 40 mg of catalyst was fixed as the optimum dosage for further reactions.

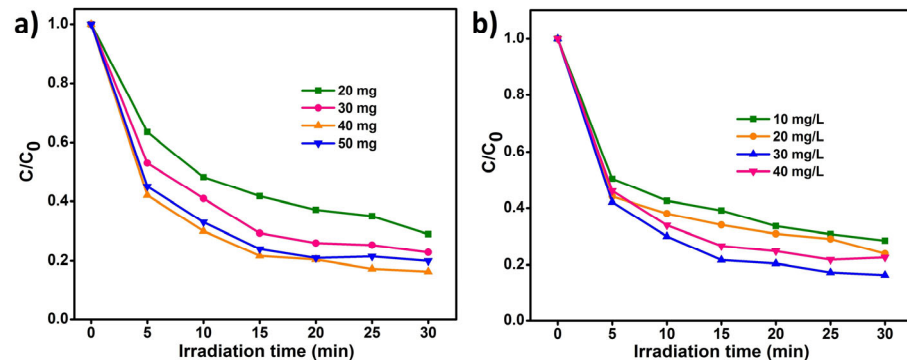


**Figure 9.** Photodegradation of MO dye at different conditions: (a) Different loading dosages of VO/GPB composite and (b) Different concentrations of MO dye in aqueous solution.

### 3.5.3. The Effectiveness of Pollutant Concentration

The role of pollutant concentration is most important for an effective photocatalytic process. Here, the concentration of MO was altered from 10 to 40 mg/L. From Figure 9b, the efficiency of the catalytic degradation reaction was suppressed, owing to the opacity of the higher concentration of pollutant (30 mg/L of MO). The higher concentration of MO reduces the penetration of the light source into the solution, which encourages a light-scattering effect. Based on this, the lower concentration of pollutants (30 mg/L of MO) shows superior catalytic efficiency compared to higher concentrations.

### 3.5.4. Effect of pH

Figure 10a shows the outcome of altering the pH of the reaction from 3 to 7 by the use of HCl (acidic medium) and NaOH (basic medium). The VO/GPB composite that reveals better catalytic activity at pH = 3 may be due to the highly protonated photocatalyst surface. The catalytic efficiency of the VO/GPB composite gradually decreased at a high pH value because the surface of the photocatalyst became more negative. As a result, the pH = 3 medium was most favorable for the photodegradation reaction of MO.

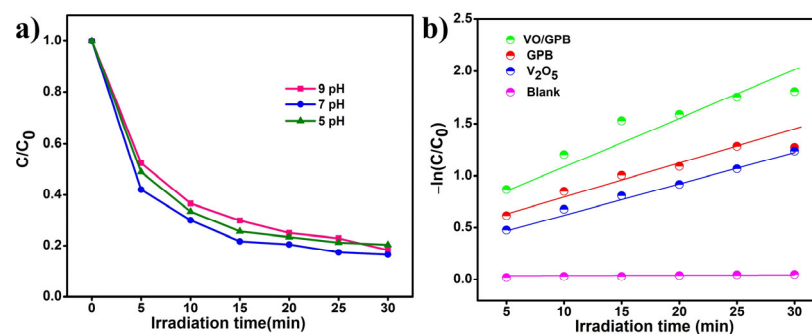


**Figure 10.** Photodegradation of MO dye with the effects of (a) various pH conditions and (b) the corresponding first-order kinetics plots for different samples.

### 3.5.5. Kinetic Studies

The kinetic studies of  $V_2O_5$  nanoblocks, GPB grits, and VO/GPB composite were performed to find the rate constant value of the degradation process, as shown in Figure 10b. The plot of the kinetic studies was drawn between time and  $\ln(C_0/C)$  value.  $V_2O_5$  nanoblocks, GPB grits, and VO/GPB composite showed rate constant values of 0.0367, 0.0385, and 0.0539  $\text{min}^{-1}$ , and the  $R^2$  values were 0.9168, 0.8202, and 0.7956, respectively. The VO/GPB composite shows higher rate constant values than the others; this is due to the photoelectric separation capacity before the renovation of pollutant irradiation.

### 3.5.6. ROS Study

The Reactive Oxidative Species (ROS) study was used to forecast the effect of scavengers in the photodegradation process. Different scavengers like TEOA, IPA, and BQ were used as quenchers for  $h^+$ ,  $\bullet O_2^-$ , and  $\bullet OH$ , respectively, to examine the main reactive species in the degradation process [46,47]. As shown in Figure 11a, upon the irradiation by visible light, the degradation of MO was decreased due to the addition of IPA and BQ as quenchers for  $\bullet OH$  and  $\bullet O_2^-$ , respectively. But a very tiny range of changes was observed, while the addition of TEOA acted as a quencher for  $h^+$ . These results prove that the  $\bullet OH$  and  $\bullet O_2^-$  radicals play a major role in the degradation of MO solution under the illumination of visible light.

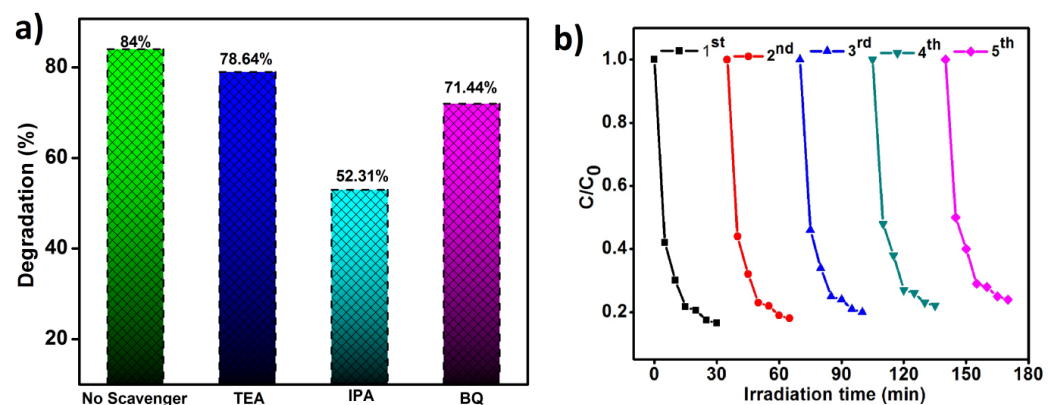
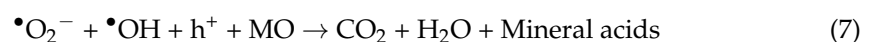
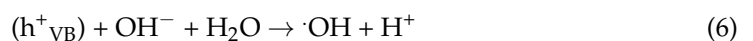
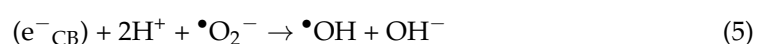
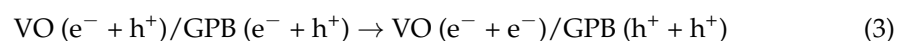


**Figure 11.** ROS study and the recycle ability analysis of VO/GPB samples: (a) Photodegradation of MO dye in the presence of various scavengers, (b) Repeatability experiments for the different reactions with the as-prepared VO/GPB nanocomposite under visible light irradiation.

### 3.5.7. Plausible Mechanism of the Photodegradation

Based on the above set of results, the mechanism of the MO degradation was predicted as follows:



Upon the irradiation by visible light, the VO/GPB composite becomes excited and generates electrons in the conduction band (CB), at the same time leaving holes ( $h_{vb}^+$ ) in the valence band, as depicted in the Equations (2) and (3). From Equation (4), the superoxide radical anion ( $\bullet O_2^-$ ) is generated by the reaction between the electrons ( $e^-$ ) and an atmospheric oxygen molecule. As shown in Equation (5), superoxide radical anions react with an excess of electrons ( $e^-$ ) and holes ( $h_{vb}^+$ ) to form hydroxyl radicals ( $\bullet OH$ ). After that, the  $h_{vb}^+$  reacts with  $\bullet OH$  and water molecules to form  $\bullet OH$  and  $H^+$  ions (Equation (6)). Finally, the superoxide radical anion ( $\bullet O_2^-$ ) reacts with  $\bullet OH$  and  $h^+$  to convert the MO pollutant into non-toxic  $CO_2$ ,  $H_2O$ , and mineral acids, as depicted in Equation (7).

### 3.5.8. Reusability Test

After the successful degradation reaction, the catalyst was collected to predict its stability and reusable capacity. Figure 11b attributes the effect of the reusability test to MO degradation within 30 min. The VO/GPB composite produces better catalytic efficiency up to the fifth cycle of degradation. If the test was raised after the fifth cycle, the efficacy of the catalyst was diminished. The efficiency of the VO/GPB composite for MO degradation was 83.86%, 81.21%, 79.91%, 77.05%, and 75.37% for five cyclical runs. This result confirms the mechanical stability and reusability properties of VO/GPB composite. Additionally, Table 1 compares VO/GPB with other catalysts for the degradation of different contaminants that have been reported. With a catalyst dose of 0.04 g/L, this also demonstrated improved performance on the 84% degradation of MO in 30 min. Alternatively, other catalysts need at least 90 min to degrade the pollutants.

**Table 1.** Comparison of degradation performance using VO/GPB with various catalysts.

S. No	Catalyst	Weight of Catalyst (g/L)	Organic Pollutant	Irradiation Light	% of Degradation	Time (min)	Source
1	TiO <sub>2</sub> -bamboo	0.05	MB	UV light	90	120	[48]
2	BiOX (X = Cl or Br)-biochar	0.05	MO	Visible light	82	150	[49]
3	g-C <sub>3</sub> N <sub>4</sub> -biochar	0.45	MB	LED light	91	240	[50]
4	Nano- $\beta$ -FeOOH/Fe <sub>3</sub> O <sub>4</sub> /Biochar	0.1	MO	Xenon lamp	98	90	[51]
5	TiO <sub>2</sub> /Fe/Fe <sub>3</sub> C/biochar	1.00	MB	UV light	89.2	300	[52]
6	Fe <sub>2</sub> O <sub>3</sub> /TiO <sub>2</sub> /biochar	2.00	MB	Visible light	75	60	[53]
			Rh		60		
7	Zn/TiO <sub>2</sub> /biochar	1.25	BMO	Visible light	40	180	[54]
			Sulfamethoxazole		80.0		
8	VO/GPB	0.04	MO	Visible light	84	30	This work

In Figure 12, we see the XRD analysis of the VO/GPB nanocomposite following the sixth cycle of MO dye degradation. The durability and recyclability of the produced nanocomposites were demonstrated by the fact that the VO/GPB photocatalyst showed only a slight drop in photocatalytic efficiency rather than a large loss after six cycles, with increased photocatalytic efficacy attained. In addition, XRD tests performed after six cycles provide conclusive evidence of the purity of the synthesized nanocomposite.

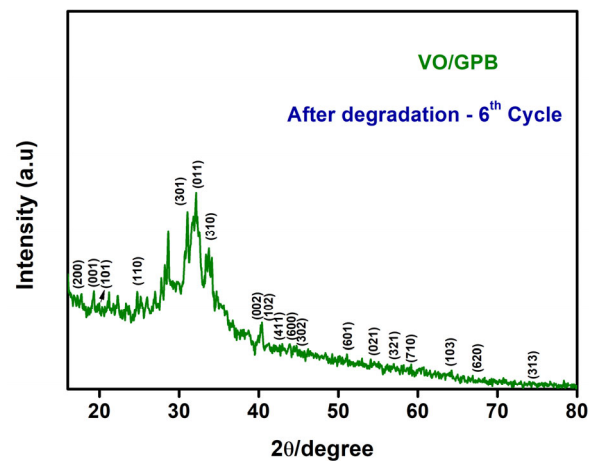


Figure 12. XRD analysis of VO/GPB nanocomposite after 6th-cycle degradation of MO dye.

### 3.6. Antioxidant Activity

According to the literature, most metal oxides have antioxidant activity and, thus, they are emerging as effective antioxidants and therapeutic reagents. In general, the hydroxyl free radical is accountable for tissue damage and is associated with inflammation; hence, the removal of this free radical is acknowledged as the main goal of antioxidant treatment [55–59]. The DPPH assay experiment was applied to examine the antioxidant activity of synthesized VO/GPB composite in the varied concentration range of 20–40 mg/L using ascorbic acid (Vitamin C) as a standard drug in this work. DPPH's radical-scavenging ability is superior, and it creates a stable free radical that can accept an electron or hydrogen [60,61]. The free radical can then be converted into a diamagnetic compound that is stable. The reaction mixture was incubated at room temperature for 30 min, and absorbance was measured at 517 nm, which showed a significant absorption band. As the electron becomes coupled, the absorption reduces, as the number of electrons taken up increases [62,63]. This type of change in absorption has long been used to assess a VO/GPB composite capacity to function as an antioxidant. These findings show that the VO/GPB composite has higher antioxidant activity compared to ascorbic acid; the scavenging effect increased with increasing concentrations of VO/GPB composite until it reached 40 mg/L, where the scavenging effect was the highest, at 93.86%, which confirms almost identical free radical inhibitory action. Figure 13 depicts the antioxidant efficacy of the VO/GPB composite. Table 2 shows the comparison report for the antioxidant activity percentage by Vitamin C and VO/GPB. From the results, VO/GPB nanocomposite has higher antioxidant activity values than the standard Vitamin C at various concentrations of VO/GPB samples.

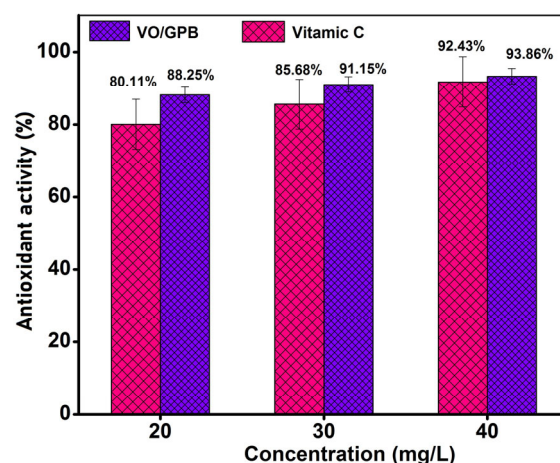


Figure 13. Percentage of antioxidant activity of VO/GPB composite using Vitamin C as standard.

**Table 2.** The antioxidants efficiency of VO/GPB composite using Vitamin C as standard.

Concentration (mg/L)	Vitamin C (%)	VO/GPB (%)
20	80.11	88.25
30	85.68	91.15
40	92.43	93.86

#### 4. Conclusions

In summary, the VO/GPB composite has been fruitfully fabricated via an easy hydrothermal path. The morphology and crystallinity of  $V_2O_5$ , GPB, and VO/GPB composite were established and characterized by PXRD, SEM with EDAX, UV-DRS, and PL analysis. From the UV-DRS investigation, the bandgap values of prepared samples were predicted, and the VO/GPB composite showed a suitable band energy value compared to bare  $V_2O_5$ . Providentially, the VO/GPB composite exhibited superior photocatalytic effectiveness in the visible light region. It showed tremendous charge carrier separation and catalytic activity towards the degradation of MO, with 84% degradation efficacy within 30 min. The VO/GPB composite demonstrated elevated stability and repeatability over five repeated runs. This study proposed a new point of view on the growth of photodegradation by utilizing a VO/GPB composite for ecological applications. In addition, the VO/GPB composite had higher antioxidant activity compared to ascorbic acid at 40 mg/L, where the radical-scavenging effect was the highest, at 93.86%. Due to their low cost, stability, efficiency, and limited impact on the environment, bio-inspired nanometal oxides have become popular as materials for environmental remediation. Metal oxides are promising for environmental cleanup because of their high catalytic capability when driven by visible light. Metal oxides have been investigated for their potential as photocatalysts in a variety of energy and environmental applications, with a focus on recent advances and future directions in this field. Hydrogen production by water splitting is crucial, as is the growth of renewable energy in general.

**Author Contributions:** Conceptualization, P.S.; methodology, P.S. and G.S.; software, T.K.; validation, T.K.; formal analysis, K.G., G.S. and T.H.O.; investigation, P.S. and K.L.; resources, K.G. and K.K.; data curation, P.S.; writing—original draft preparation, P.S.; writing—review and editing, G.S. and K.K.; visualization, T.H.O.; supervision, G.S.; project administration, T.H.O.; funding acquisition, T.H.O. All authors have read and agreed to the published version of the manuscript.

**Funding:** We sincerely thank the National Research Foundation of Korea (NRF) grant (No. 2022R1A2C1004283) funded by the Korean government (MSIT).

**Institutional Review Board Statement:** Not applicable.

**Informed Consent Statement:** Not applicable.

**Data Availability Statement:** Not applicable.

**Acknowledgments:** Karthik Kannan is grateful to Ariel University for offering a postdoctoral fellowship.

**Conflicts of Interest:** The authors declare no conflict of interest.

#### References

- Mitra, M.; Aziz, H.Y. Decoration of  $Fe_3O_4$  and  $CoWO_4$  nanoparticles over graphitic carbon nitride: Novel visible-light-responsive photocatalysts with exceptional photocatalytic performances. *Mater. Res. Bull.* **2018**, *105*, 159–171.
- Akbar, M.; Kshipra, K.; Shaikh, M.M. Improved Photocatalytic Degradation of Organic Dyes by ZnO-Nanoflowers. *ChemistrySelect* **2016**, *1*, 3483–3490.
- Cheng, C.; Zhang, J.; Zhang, C.; Liu, H.; Liu, W. Preparation and characterization of charcoal from feathers and its application in trimethoprim adsorption. *Desalination Water Treat.* **2014**, *52*, 5401–5412. [[CrossRef](#)]
- Teng, Z.; Han, K.; Li, J.; Gao, Y.; Li, M.; Ji, T. Ultrasonic-assisted preparation and characterization of hierarchical porous carbon derived from garlic peel for high-performance supercapacitors. *Ultrason. Sonochem.* **2020**, *60*, 104756. [[CrossRef](#)] [[PubMed](#)]

5. Ashtaputrey, P.D.; Ashtaputrey, S.D. Preparation and characterization of activated charcoal derived from wood apple fruit shell. *J. Sci. Res.* **2020**, *64*, 336–340. [[CrossRef](#)]
6. Rotami, M.; Hamadianian, M.; Nasrabadi, M.R.; Ganjali, R. Sol–gel preparation of metal and nonmetal-codoped TiO<sub>2</sub>-graphene nanophotocatalyst for photodegradation of MO under UV and visible-light irradiation. *Ionics* **2019**, *25*, 1869–1878. [[CrossRef](#)]
7. Jung, E.L.; Young, K.P. Applications of modified biochar-based materials for the removal of environment pollutants: A Mini Review. *Sustainability* **2020**, *12*, 6112.
8. Fadhil, O.H.; Eisa, M.Y. Removal of methyl orange from aqueous solutions by adsorption using corn leaves as adsorbent material. *J. Eng.* **2019**, *25*, 55–69. [[CrossRef](#)]
9. Hasanpour, M.; Motahari, S.; Jing, D.; Hatami, M. Statistical analysis and optimization of photodegradation efficiency of methyl orange from aqueous solution using cellulose/zinc oxide hybrid aerogel by response surface methodology (RSM). *Arab. J. Chem.* **2021**, *14*, 103401. [[CrossRef](#)]
10. Kalyani, P.; Anitha, A. Refuse derived energy—Tea derived boric acid activated carbon as an electrode material for electrochemical capacitors. *Port. Electrochim. Acta* **2013**, *31*, 165–174. [[CrossRef](#)]
11. Rasheed, R.T.; Mansoor, H.S.; Abdullah, T.A.; Tatjana, J.; Noor, A.J.; Ali, D.S.; Rasha, R.S. Synthesis, characterization of V<sub>2</sub>O<sub>5</sub> nanoparticles and determination of catalase mimetic activity by new colorimetric method. *J. Therm. Anal. Calorim.* **2021**, *145*, 297–307. [[CrossRef](#)]
12. Subhash, C.; Pravin, J.; Isha, M.; Ashwani, K.T.; Mattia, B.; Antonio, D.N.; Fabrizio, O. Biochar-supported TiO<sub>2</sub>-based nanocomposites for the photocatalytic degradation of sulfamethoxazole in water—A review. *Toxics* **2021**, *9*, 313.
13. Liu, X.; Zeng, J.; Yang, H.; Zhou, K.; Pan, D. V<sub>2</sub>O<sub>5</sub>-Based nanomaterials: Synthesis and their applications. *RSC Adv.* **2018**, *8*, 4014–4031. [[CrossRef](#)]
14. Guillaume, S.; Brice, B.; Issam, M.; Manuel, G.; Aline, R. Polyol Synthesis of Ti-V<sub>2</sub>O<sub>5</sub> nanoparticles and their use as electrochromic films. *Inorg. Chem.* **2016**, *55*, 9838–9847.
15. Huang, X.; Zhu, S.; Zhang, H.; Huang, Y.; Wang, X.; Wang, Y.; Chen, D. Biochar nanoparticles induced distinct biological effects on freshwater algae via oxidative stress, membrane damage, and nutrient depletion. *ACS Sustain. Chem. Eng.* **2021**, *9*, 10761–10770. [[CrossRef](#)]
16. Chen, X.; Duan, M.; Zhou, B.; Cui, L. Effects of biochar nanoparticles as a soil amendment on the structure and hydraulic characteristics of a sandy loam soil. *Soil Use Manag.* **2022**, *38*, 836–849. [[CrossRef](#)]
17. Tan, X.-F.; Liu, Y.-G.; Gu, Y.-L.; Xu, Y.; Zeng, G.-M.; Hu, X.-J.; Liu, S.-B.; Wang, X.; Liu, S.-M.; Li, J. Biochar-based nano-composites for the decontamination of wastewater: A review. *Bioresour. Technol.* **2016**, *212*, 318–333. [[CrossRef](#)] [[PubMed](#)]
18. Patryk, O.; Wiesława, C.B.; Aleksandra, B.; Ewa, S.; Yong, S.O. Characterization of nanoparticles of biochars from different biomass. *J. Anal. Appl. Pyrolysis* **2016**, *121*, 165–172.
19. Neha, C.; Jyoti, S.; Ram, P. Nanobiochar and biochar-based nanocomposites: Advances and applications. *J. Sci. Food Agric.* **2021**, *5*, 100191.
20. Zhu, K.; Meng, Y.; Qiu, H.; Gao, Y.; Wang, C.; Du, F.; Wei, Y.; Chen, G.; Wang, C.; Chen, G. Facile synthesis of V<sub>2</sub>O<sub>5</sub> nanoparticles as a capable cathode for high energy lithium-ion batteries. *J. Alloys Compd.* **2015**, *50*, 370–373. [[CrossRef](#)]
21. Karthik, K.; Dhanuskodi, S.; Gobinath, C. Dielectric and antibacterial studies of microwave assisted calcium hydroxide nanoparticles. *J. Mater. Sci. Mater. Electron.* **2015**, *28*, 16509–16518. [[CrossRef](#)]
22. Revathi, V.; Karthik, K. Physico-chemical properties and antibacterial activity of Hexakis (Thiocarbamide) Nickel(II) nitrate single crystal. *Chem. Data Collect.* **2019**, *21*, 100229. [[CrossRef](#)]
23. Kannan, K.; Radhika, D.; Nesaraj, A.S.; Sadasivuni, K.K.; Krishna, L.S. Facile synthesis of NiO-CYSO nanocomposite for photocatalytic and antibacterial applications. *Inorg. Chem. Commun.* **2020**, *122*, 108307. [[CrossRef](#)]
24. Majid, F.; Nilofar, A. Chemical synthesis of vanadium oxide (V<sub>2</sub>O<sub>5</sub>) nanoparticles prepared by sodium metavanadate. *J. Nanomed. Res.* **2017**, *5*, 00103.
25. Zahra, A.H.; Rashed, T.R. Preparation of V<sub>2</sub>O<sub>5</sub> and SnO<sub>2</sub> Nanoparticles and their application as pollutant removal. *J. Nanotechnol.* **2021**, *1*, 69–80.
26. Karthik, K.; Maria, P.N.; Anukorn, P.; Pushpa, S.; Revathi, V.; Subbulakshmi, M. Ultrasound-assisted synthesis of V<sub>2</sub>O<sub>5</sub> nanoparticles for photocatalytic and antibacterial studies. *Mater. Res. Innov.* **2020**, *24*, 229–234. [[CrossRef](#)]
27. Shreenivasa, L.; Yogeeshwari, R.T.; Viswanatha, R.; Sriram, G.; Kalegowda, Y.; Kurkuri Mahaveer, D.; Ashoka, S. An introduction of new nanostructured Zn<sub>0.29</sub>V<sub>2</sub>O<sub>5</sub> cathode material for lithium ion battery: A detailed studies on synthesis, characterization and lithium uptake. *Mater. Res. Exp.* **2019**, *6*, 115035. [[CrossRef](#)]
28. Salam, A.M.; Lamy, A.A.; Emad, Y.; Ali, A.A.; Fazal, M.; Hazim, F.A.; Sausan, A. Synthesis of NiO:V<sub>2</sub>O<sub>5</sub> nanocomposite and its photocatalytic efficiency for methyl orange degradation. *Heliyon* **2018**, *4*, 00581.
29. Guo, F.; Bao, L.; Wang, H.; Larson, S.L.; Ballard, J.H.; Knotek-Smith, H.M.; Zhang, Q.; Su, Y.; Wang, X.; Han, F. A simple method for the synthesis of biochar nanodots using hydrothermal reactor. *MethodsX* **2020**, *7*, 101022. [[CrossRef](#)]
30. Hunge, Y.M.; Yadav, A.A.; Mathe, V.L. Ultrasound assisted synthesis of WO<sub>3</sub>-ZnO nanocomposites for brilliant blue dye degradation. *Ultrason. Sonochem.* **2018**, *45*, 116–122. [[CrossRef](#)]
31. Babu, S.G.; Vinoth, R.; Kumar, D.P.; Shankar, M.V.; Chou, H.L.; Vinodgopal, K.; Neppolian, B. The influence of electron storing, transferring and shuttling on reduced graphene oxide at the interfacial copper doped TiO<sub>2</sub> p-n heterojunction for increased hydrogen production. *Nanoscale* **2015**, *7*, 7849–7857. [[CrossRef](#)] [[PubMed](#)]

32. Sivaganesh, D.; Saravanakumar, S.; Sivakumar, V.; Rajajeyaganthan, R.; Arunpandian, M.; Nandha Gopal, J.; Thirumalaisamy, T.K. Surfactants-assisted synthesis of ZnWO<sub>4</sub> nanostructures: A view on photocatalysis, photoluminescence and electron density distribution analysis. *Mater. Charact.* **2020**, *159*, 110035. [[CrossRef](#)]
33. Tan, X.F.; Liu, Y.G.; Zeng, G.; Wang, X.; Hu, X.; Gu, Y.; Yang, Z. Application of biochar for the removal of pollutants from aqueous solutions. *Chemosphere* **2015**, *125*, 70–85. [[CrossRef](#)] [[PubMed](#)]
34. Yao, Y.; Gao, B.; Chen, J.; Yang, L. Engineered biochar reclaiming phosphate from aqueous solutions: Mechanisms and potential application as a slowrelease fertilizer. *Environ. Sci. Technol.* **2013**, *47*, 8700–8708. [[CrossRef](#)] [[PubMed](#)]
35. Yao, Y.; Gao, B.; Inyang, M.; Zimmerman, A.R.; Cao, X.; Pullammanappallil, P.; Yang, L. Biochar derived from anaerobically digested sugar beet tailings: Characterization and phosphate removal potential. *Bioresour. Technol.* **2011**, *102*, 6273–6278. [[CrossRef](#)]
36. Zhang, M.; Gao, B.; Varnoosfaderani, S.; Hebard, A.; Yao, Y.; Inyang, M. Preparation and characterization of a novel magnetic biochar for arsenic removal. *Bioresour. Technol.* **2013**, *130*, 457–462. [[CrossRef](#)]
37. Inyang, M.; Gao, B.; Zimmerman, A.; Zhang, M.; Chen, H. Synthesis, characterization, and dye sorption ability of carbon nanotube–biochar nanocomposites. *Chem. Eng. J.* **2014**, *236*, 39–46. [[CrossRef](#)]
38. Naghdi, M.; Taheran, M.; Brar, S.K.; Kermanshahi-Pour, A.; Verma, M.; Surampalli, R.Y. Pinewood nanobiochar: A unique carrier for the immobilization of crude laccase by covalent bonding. *Int. J. Biol. Macromol.* **2018**, *115*, 563–571. [[CrossRef](#)]
39. Younas, U.; Gulzar, A.; Ali, F.; Pervaiz, M.; Ali, Z.; Khan, S.; Saeed, Z.; Ahmed, M.; Alothman, A.A. Antioxidant and Organic Dye Removal Potential of Cu-Ni Bimetallic Nanoparticles Synthesized Using *Gazania rigens* Extract. *Water* **2021**, *13*, 2653. [[CrossRef](#)]
40. Younas, U.; Hassan, S.T.; Ali, F.; Hassan, F.; Saeed, Z.; Pervaiz, M.; Khan, S.; Jannat, F.T.; Bibi, S.; Sadiqa, A.; et al. Radical Scavenging and Catalytic Activity of Fe-Cu Bimetallic Nanoparticles Synthesized from *Ixora finlaysoniana* Extract. *Coatings* **2021**, *11*, 813. [[CrossRef](#)]
41. Imran, M.; Saeed, Z.; Pervaiz, M.; Mehmood, K.; Ejaz, R.; Younas, U.; Nadeem, H.A.; Hussain, S. Enhanced visible light photocatalytic activity of TiO<sub>2</sub> co-doped with Fe, Co, and S for degradation of Congo red. *Spectrochim. Acta Part A Mol. Biomol. Spectrosc.* **2021**, *255*, 119644. [[CrossRef](#)] [[PubMed](#)]
42. Kosta, I.; Navone, C.; Bianchin, A.; García-Lecina, E.; Grande, H.; Ihou Mouko, H.; Azpeitia, J.; García, I. Influence of vanadium oxides nanoparticles on thermoelectric properties of an N-type Mg<sub>2</sub>Si<sub>0.888</sub>Sn<sub>0.1</sub>Sb<sub>0.012</sub> alloy. *J. Alloys Compd.* **2021**, *856*, 158069. [[CrossRef](#)]
43. Mahalingam, S.; Ali, A.; Abdulaziz, A.; Ramasamy, J. Enhanced photocatalytic performance of the graphene-V<sub>2</sub>O<sub>5</sub> nanocomposite in the degradation of methylene blue dye under direct sunlight. *Appl. Mater. Interfaces* **2015**, *7*, 14905–14911.
44. Martha, S.; Das, D.P.; Biswala, N.; Parida, K.M. Facile synthesis of visible light responsive V<sub>2</sub>O<sub>5</sub>/N, S-TiO<sub>2</sub> composite photocatalyst: Enhanced hydrogen production and phenol degradation. *J. Mater. Chem.* **2012**, *22*, 10695–10703. [[CrossRef](#)]
45. Mandal, R.K.; Kundu, S.; Sain, S.; Pradhan, S.K. Enhanced photocatalytic performance of V<sub>2</sub>O<sub>5</sub>-TiO<sub>2</sub> nanocomposites synthesized by mechanical alloying with morphological hierarchy. *New J. Chem.* **2019**, *43*, 2804–2816. [[CrossRef](#)]
46. Liao, Y.; Jia, L.; Chen, R.; Gu, O.; Sakurai, M.; Kameyama, H.; Zhou, L.; Ma, H.; Guo, Y. Charcoal-supported catalyst with enhanced thermal-stability for the catalytic combustion of volatile organic compounds. *Appl. Catal. A Gen.* **2016**, *522*, 32–39. [[CrossRef](#)]
47. Tuokko, S.; Pihko, P.M. Palladium on charcoal as a catalyst for stoichiometric chemo- and stereoselective hydrosilylations and hydrogenations with triethylsilane. *Org. Process Res. Dev.* **2014**, *18*, 1740–1751. [[CrossRef](#)]
48. Wu, F.; Liu, W.; Qiu, J.; Li, J.; Zhou, W.; Fang, Y.; Zhang, S.; Li, X. Enhanced photocatalytic degradation and adsorption of methylene blue via TiO<sub>2</sub> nanocrystals supported on graphene-like bamboo charcoal. *Appl. Surf. Sci.* **2015**, *358*, 425–435. [[CrossRef](#)]
49. Li, M.; Huang, H.; Yu, S.; Tian, N.; Dong, F.; Du, X.; Zhang, Y. Simultaneously promoting charge separation and photoabsorption of BiOX (X = Cl, Br) for efficient visible-light photocatalysis and photosensitization by compositing low-cost biochar. *Appl. Surf. Sci.* **2016**, *386*, 285–295. [[CrossRef](#)]
50. Pi, L.; Jiang, R.; Zhou, W.; Zhu, H.; Xiao, W.; Wang, D.; Mao, X. g-C<sub>3</sub>N<sub>4</sub> Modified biochar as an adsorptive and photocatalytic material for decontamination of aqueous organic pollutants. *Appl. Surf. Sci.* **2015**, *358*, 231–239. [[CrossRef](#)]
51. Zhang, Z.; Wang, G.; Li, W.; Zhang, L.; Guo, B.; Ding, L.; Li, X. Photocatalytic Activity of Magnetic Nano-β-FeOOH/Fe<sub>3</sub>O<sub>4</sub>/Biochar Composites for the Enhanced Degradation of Methyl Orange Under Visible Light. *Nanomaterials* **2021**, *11*, 526. [[CrossRef](#)] [[PubMed](#)]
52. Mian, M.M.; Liu, G. Sewage Sludge-Derived TiO<sub>2</sub>/Fe/Fe<sub>3</sub>C-Biochar Composite as an Efficient Heterogeneous Catalyst for Degradation of Methylene Blue. *Chemosphere* **2019**, *215*, 101–114. [[CrossRef](#)] [[PubMed](#)]
53. Chen, X.L.; Li, F.; Chen, H.; Wang, H.; Li, G. Fe<sub>2</sub>O<sub>3</sub>/TiO<sub>2</sub> Functionalized Biochar as a Heterogeneous Catalyst for Dyes Degradation in Water under Fenton Processes. *J. Environ. Chem. Eng.* **2020**, *8*, 103905. [[CrossRef](#)]
54. Xie, X.; Li, S.; Zhang, H.; Wang, Z.; Huang, H. Promoting Charge Separation of Biochar-Based Zn-TiO<sub>2</sub>/PBC in the Presence of ZnO for Efficient Sulfamethoxazole Photodegradation under Visible Light Irradiation. *Sci. Total Environ.* **2019**, *659*, 529–539. [[CrossRef](#)]
55. Gala, V.; Lopez-Penalver, J.J.; Sanchez-Polo, M.; Rivera-Utrilla, J. Activated carbon as photocatalyst of reactions in aqueous phase. *Appl. Catal. B* **2013**, *142–143*, 694–704. [[CrossRef](#)]

56. Bhosale, T.T.; Shinde, H.M.; Gavade, N.L.; Babar, S.B.; Gawade, V.V.; Sabale, S.R.; Kamble, R.J.; Shirke, B.S.; Garadkar, K.M. Biosynthesis of SnO<sub>2</sub> nanoparticles by aqueous leaf extract of *Calotropis gigantea* for photocatalytic applications. *J. Mater. Sci. Mater. Electron.* **2018**, *29*, 6826–6834. [[CrossRef](#)]
57. Blinov, A.V.; Kachanov, M.D.; Gvozdenko, A.A.; Nagdalian, A.A.; Blinova, A.A.; Rekhman, Z.A.; Golik, A.B.; Vakalov, D.S.; Maglakelidze, D.G.; Nagapetova, A.G.; et al. Synthesis and Characterization of Zinc Oxide Nanoparticles Stabilized with Biopolymers for Application in Wound-Healing Mixed Gels. *Gels* **2023**, *9*, 57. [[CrossRef](#)]
58. Abdollahi, Z.; Zare, E.N.; Salimi, F.; Goudarzi, I.; Tay, F.R.; Makvandi, P. Bioactive Carboxymethyl Starch-Based Hydrogels Decorated with CuO Nanoparticles: Antioxidant and Antimicrobial Properties and Accelerated Wound Healing In Vivo. *Int. J. Mol. Sci.* **2021**, *22*, 2531. [[CrossRef](#)]
59. Gvozdenko, A.A.; Siddiqui, S.A.; Blinov, A.V.; Golik, A.B.; Nagdalian, A.A.; Maglakelidze, D.G.; Statsenko, E.N.; Pirogov, M.A.; Blinova, A.A.; Sizonenko, M.N.; et al. Synthesis of CuO nanoparticles stabilized with gelatin for potential use in food packaging applications. *Sci. Rep.* **2022**, *12*, 12843. [[CrossRef](#)]
60. Jyoti, P.S.; Samrat, P.; Bolin, K.K.; Sanjoy, K.S. Ultrasonication: Enhances the antioxidant activity of metal oxide nanoparticles. *Colloids Surf. B Biointerfaces* **2010**, *79*, 521–523.
61. Sandhya, J.; Kalaiselvam, S. Biogenic synthesis of magnetic iron oxide nanoparticles using inedible borassusflabellifer seed coat: Characterization, antimicrobial, antioxidant activity and in vitro cytotoxicity analysis. *Mater. Res. Express* **2020**, *7*, 015045. [[CrossRef](#)]
62. Ekpete, O.A.; Marcus, A.C.; Osi, V. Preparation and Characterization of Activated Carbon Obtained from Plantain (*Musa paradisiaca*) Fruit Stem. *J. Chem.* **2017**, *2017*, 8635615. [[CrossRef](#)]
63. Burcu, S.T.; Tugce, F.; Pelin, T.; Bijen, K.; Besra, O.Y.; Cagla, K.; Sunde, Y.S.; Cumhur, G. Structural characterization, antioxidant and cytotoxic effects of iron nanoparticles synthesized using *Asphodelus aestivus* brot. aqueous extract. *Green Synth. Catal.* **2020**, *9*, 153–163.

**Disclaimer/Publisher's Note:** The statements, opinions and data contained in all publications are solely those of the individual author(s) and contributor(s) and not of MDPI and/or the editor(s). MDPI and/or the editor(s) disclaim responsibility for any injury to people or property resulting from any ideas, methods, instructions or products referred to in the content.